

Dedicated to

My

Beloved Parents

DECLARATION

I hereby declare that the thesis entitled on “**Metal-free and Transition Metal Complex Mediated Synthetic Approaches towards the Development of Bioactive Compounds**” submitted for the award of Ph.D. Degree, is the result of investigations carried out by me at Department Chemistry, University of North Bengal under the supervision of Professor Bhaskar Biswas and further that no portion of this thesis has ever used as the foundation for the award of a any degree or fellowship.

Rajani Kanta Mahato.
.....

RAJANI KANTA MAHATO

Department of Chemistry

University of North Bengal

Darjeeling-734013

West Bengal, India

Date: 15/5/2023



समानो मन्त्रः समितिः समानी

University of North Bengal

A STATE GOVERNMENT AIDED UNIVERSITY

Dr. Bhaskar Biswas, Professor, Dept. of Chemistry

CERTIFICATE

I declare that **Mr. RAJANI KANTA MAHATO** has prepared the thesis entitled of **“Metal-free and Transition Metal Complex Mediated Synthetic Approaches towards the Development of Bioactive Compounds”** for the award of Ph.D. degree of University of North Bengal, under my supervision. He has completed his thesis work at the Department of Chemistry, University of North Bengal.

.....
Prof. Bhaskar Biswas

Department of Chemistry
University of North Bengal
Darjeeling-734013
West Bengal, India

Date: **BHASKAR BISWAS**
Professor

Department of Chemistry
University of North Bengal
Darjeeling – 734 013 (W.B.)

Raja Rammohunpur – 734 013, Dist. Darjeeling, West Bengal, INDIA.

Website: <http://www.nbu.ac.in>,





Email: bhaskarbiswas@nbu.ac.in

Mob. 9477089710 / 7003372248

Document Information

Analyzed document: Rajani Kanta Mahato_Chemistry.pdf (D166541077)
Submitted: 2023-05-11 08:47:00
Submitted by: University of North Bengal
Submitter email: nbuplg@nbu.ac.in
Similarity: 2%
Analysis address: nbuplg.nbu@analysis.arkund.com


Sources included in the report

W	URL: https://pubs.rsc.org/en/content/articlehtml/2018/ra/c7ra12104k Fetched: 2019-10-30 01:19:31		6
W	URL: http://scripts.iucr.org/cgi-bin/paper?lh4048 Fetched: 2021-11-16 14:56:55		6
W	URL: http://www.rsc.org/suppdata/ob/b6/b612776m/b612776m.pdf Fetched: 2021-10-11 20:34:30		5
W	URL: https://vdoc.pub/documents/organophosphorus-chemistry-vol-40-7kq55sksjl00 Fetched: 2021-11-09 05:35:58		1

Entire Document

Metal-free and Transition Metal Complex Mediated Synthetic Approaches towards the Development of Bioactive Compounds Thesis submitted to University of North Bengal in partial fulfillment of the requirements for the degree of Doctor of Philosophy in Chemistry By Mr. RAJANI KANTA MAHATO (M.Sc. in Chemistry) Supervised by Prof. BHASKAR BISWAS DEPARTMENT OF CHEMISTRY UNIVERSITY OF NORTH BENGAL DARJEELING -734013 WEST BENGAL, INDIA
May 2023

Rajani Kanta Mahato.
15/5/2023


DR. BHASKAR BISWAS
Professor
Department of Chemistry
University of North Bengal
Darjeeling - 734 013 (W.B.)

PREFACE

The journey of my research work related to my doctoral degree thesis entitled “**Metal-free and Transition Metal Complex Mediated Synthetic Approaches Towards the Development of Bioactive Compounds**” started in the year 2018 under the supervision of Dr. Bhaskar Biswas of the department of Chemistry at Surendranath College, Calcutta University, West Bengal, India. Later, I shifted to the University of North Bengal as a State fellow as Dr. Biswas joined to the Department of Chemistry, University of North Bengal. I admitted to the Ph.D. course work in January 2020 and successfully completed the same with CGPA 9.60 on 5th February 2021. I have been registered for the Ph.D. degree which effect from 2nd January 2020 with vides Ref. No. Ph.D/Chem. (1347) / 569 / R-2021.

Bioactive compounds are highly significant for their huge medicinal applications. Therefore, lots of research has been going on for the development of the bioactive compounds from a long time.

The current study deals with the production of the value-added bioactive compounds through the newly synthesized transition metal complex and metal-free synthetic routes. A variety of spectroscopic and analytical techniques, as well as single crystal X-ray diffraction examinations, have been used to characterise the synthesized compounds. Detail theoretical calculations using the Density Functional Theory (DFT) have been used to further correlate the structural characteristics with the theoretical possibilities and for the proposed mechanisms of the reaction. Finally, the future direction of the exploration has been defined with respect to current scientific and industrial relevant.

Acknowledgement

First and foremost, I want to express my gratitude to God, the Almighty, for giving me the blessings for this long journey.

I would like to take this opportunity to express my sincere gratitude and debt of gratitude to my supervisor, Prof. Bhaskar Biswas, whose wise counsel, constant support, outstanding supervision, and care give me the freedom to conduct my research in a wonderful environment. I successfully overcame several challenges and learned a lot under his guidance. He has been the source of my unending inspiration as I have persevered down this wonderful doctoral study.

I want to extend my profound gratitude to Prof. Biswajit Sinha, Head of the Department of Chemistry at the University of North Bengal, for providing the administrative assistance and facilities I needed to complete my research. I greatly appreciate the assistance provided by all other faculty members and the department's non-teaching staff during the research phase.

For his prompt assistance and cooperation with Single Crystal X-ray diffraction experiments, I would like to express my gratitude to Dr. Angshuman Roy Choudhury of the Department of Chemical Sciences at the Indian Institute of Science Education and Research (IISER) Mohali. Additionally, I would like to express my gratitude to our esteemed national and international collaborators for providing me with invaluable experimental and theoretical support during my research study.

I am thankful to all my lab mates, especially Dr. Prafulla Kumar Mudi, Mr. Chanchal Kumar Pal, Mr. Suvojit Roy, Ms. Shreya Mahato, Mr. Subham Mukherjee, Mr. Sangharaj Diyali, Mr. Subhajit Saha, Mr. Subhankar Kundu, Ms. Ananya Debnath, Mr. Nilankar Diyali, Ms. Meena Chettri and all other research scholars of the department. I am also thankful to everyone who helped me, directly or indirectly to complete my research.

Finally, I express my heartfelt gratitude to my parents and my other family members for their unwavering love and support throughout this journey.

LIST OF TABLES

Table	Page No.
Table II.1. Elemental analysis of Complex 1.....	19
Table II.2. Infrared spectral data of complex 1.....	24
Table II.3. UV-Vis data of Complex 1.....	25
Table II.4. Crystallographic refinement parameters of Complex 1.....	26
Table II.5. Selected bond lengths (Å) and bond angles (°) for complex 1.....	27
Table II.6. Cartesian coordinate values and atom connectivity of the optimized complex 1 in vacuum.....	29
Table III.1. Elemental analysis of Complex 2.....	48
Table III.2. Infrared spectral data ^a of complex 2.....	51
Table III.3. UV-Vis spectral data ^a of complex 2.....	52
Table III.4. ESI-MS spectral data ^a of complex 2.....	53
Table III.5. Crystallographic data and structure refinement parameter of Complex 2 and compound 1(DAP).....	56
Table III.6. Selected bond distances and bond angles of complex 2.....	57
Table III.7. Hydrogen bond parameters donor/acceptor scheme (Å,°) for complex 2...58	
Table III.8. Selected bond lengths (Å) and bond angles (°) for DAPH ⁺ Cl ⁻ (compound 1)	61
Table III.9. Hydrogen bond parameters donor/acceptor scheme (Å,°) for DAPH ⁺ Cl ⁻ (compound 1).....	62
Table IV.1. Elemental analysis of DAPH ⁺ Cl ⁻	85
Table IV.2. Infrared spectral data of DAPH ⁺ Cl ⁻	91
Table IV.3. UV-Vis data of DAPH ⁺ Cl ⁻	92
Table IV.4. Crystallographic data and structure refinement parameters for hydrated DAPH ⁺ Cl ⁻	94
Table IV.5. Selected bond lengths (Å) and bond angles (°) for DAPH ⁺ Cl ⁻	95
Table IV.6. Hydrogen bond parameters donor/acceptor scheme (Å,°) for DAPH ⁺ Cl ⁻	97
Table IV.7. Interaction energies involved in the structure of DAPH ⁺ Cl ⁻	98
Table IV.8. Hirshfeld surface plot and fingerprint plot of DAPH ⁺ Cl ⁻	101

Table IV.9. Antibacterial activity of DAPH ⁺ Cl ⁻ and tetracycline against clinical microorganism.....	102
Table IV.10. In vitro inhibition activity B1, phenazine and remdesivirviral on 1×10e4 VeroE6 cells.....	104
Table IV.11. Molecular docking interactions of DAPH ⁺ Cl ⁻ and Mpro, nsp2 and nsp7-nps8.....	107
Table IV.12. The prediction of the ADME values for DAPH ⁺ Cl ⁻	108
Table V.1. Optimization of reaction conditions.....	130
Table V.2. Effect of equivalents of aldehyde (Stoichiometry).....	132
Table VI.1. Elemental analysis of Schiff bases.....	172
Table VI.2. Infrared spectral data ^a of H ₂ L ¹ and H ₂ L ²	176
Table VI.3. IR stretching frequencies of free β-CD and the encapsulated Complexes.....	177
Table VI.4. ¹ H chemical shifts of free β-CD and the encapsulated complexes in DMSO-d ⁶	182
Table VI.5. Crystallographic refinement parameter of H ₂ L ¹ and H ₂ L ²	195
Table VI.6. Selected bond lengths (Å) and bond angles (°) for H ₂ L ¹ obtained from X-ray structure.....	196
Table VI.7. Selected bond lengths (Å) and bond angles (°) for H ₂ L ² obtained from X-ray structure.....	197
Table VI.8. Non-covalent interaction parameter for H ₂ L ¹ Hydrogen bond parameters donor/acceptor scheme (Å°) for H ₂ L ¹	198
Table VI.9. Non-covalent interaction parameter for H ₂ L ² Hydrogen bond parameters donor/acceptor scheme (Å°) for H ₂ L ²	199
Table VI.10. <i>In vitro</i> cytotoxic activity of H ₂ L ¹ -β-CD & H ₂ L ² -β-CD against MCF-7 and MDA-MB-231.....	208

LIST OF FIGURES

Figure	Page No.
Fig. II.1. IR spectrum of complex 1.....	25
Fig. II.2. Thermal ellipsoidal diagram of complex 1.....	26
Fig. II.3. Optimized structure of the complex 1 in vacuum	28
Fig. II.4. Superimposed optimized and XRD structure of complex 1.....	29
Fig. II.5. Frontier orbitals' diagram for complex 1.....	30
Fig. II.6. MEP plot of complex 1 in vacuum (The numeric values designate the terminal colors with color range)	31
Fig. II.7. Images of the characteristic fingerprint plots of Complex 1 with their elemental contribution.....	32
Fig. II.8. Hirshfeld surface plot and fingerprint plot (all in-all out) of complex 1.....	32
Fig. II.9. Rise of an optical band at 441 nm for the growth of APX in solution upon addition of complex 1 to 100 equivalents of OPD in acetonitrile medium. (The spectra are recorded after every 5 min). Inset: Time vs Absorbance plot at defined wavelength.....	34
Fig. II.10. ESI mass spectrum of complex 1 in presence of OPD in MeOH.....	34
Fig. II.11. Rate vs conc. of OPD plot in MeOH.....	35
Fig. II.12. Inhibitory effects of complex 1 and streptomycin against pathogenic bacteria using well diffusion assay	37
Fig. II.13. Minimum inhibitory concentration of various compounds against <i>S. aureus</i> using RMA	38
Fig. II.14. Dose dependent cytotoxic effect of complex 1 on A549 cell lines after 24h incubation	38
Fig. II.15. AO/EB and Hoechst studies of complex 1 against A549 cancerous cell lines and JC-1 staining applied to <i>Staphylococcus aureus</i> for trans-membrane potential activity. Control, complex 1 untreated cells.....	40
Fig. II.16. a) (Left) Percentage of normal, apoptosis and necrosis cells in control and complex 1 treated A549 cells from AO/EB staining. b) (Right) Percentage of normal and abnormal cells from hoechst staining.....	40
Fig. III.1. FT-IR spectrum of the complex 2	51
Fig. III.2. UV-Vis spectrum of complex 2	52

Fig. III.3. ESI–MS spectrum of complex 2.....	53
Fig.III.4. ¹ H NMR spectrum of complex 2	54
Fig. III.5a ORTEP diagram of the asymmetric unit of complex 2 with 30% ellipsoidal probability. H atoms are omitted for clarity; Fig. III.5b C–H...N and π ... π interactions mediated 1D chain of dimeric complex 2 units along <i>ac</i> plane where chloride ions act as strong linker between two 1D chains of complex 2 through strong C–H...Cl and N–H...Cl interactions leading to a supramolecular architecture along <i>ac</i> plane.....	55
Fig. III.6. View of Hirshfeld surfaces of complex 2 mapped over d_{norm} , shape index, curvedness and fragment patch.....	59
Fig. III.7. 2D fingerprint plots of complex 2 with the contribution of interacting elements.....	59
Fig. III.8. a) Thermal ellipsoidal plot of the oxidation product, hydrated DAPH ⁺ Cl ⁻ (compound 1); (b) Formation of a unique type of (H ₂ O) ₆ ...(Cl) ₂ cluster leading to a layer structure of 2; (c) Dominant intermolecular H...O and O...Cl interactions mediated construction of supramolecular architecture 2 along <i>bc</i> plane; (d) π ... π interactions developing AB...AB type layer formation.....	61
Fig. III.9. A view of Hirshfeld surfaces of DAPH ⁺ mapped over d_{norm} , shape index, curvedness and fragment patch.....	63
Fig. III.10. 2D fingerprint plots of DAPH ⁺ with the contribution of interacting elements.....	63
Fig. III.11. Optimized molecular structures of cobalt(III) complex, oxidation product and reactive intermediates. H's associated with dpa in cobalt(III) complex are omitted for clarity. Here grey, blue, sky blue and white spheres represent carbon, nitrogen, cobalt and hydrogen atoms respectively	64
Fig. III.12. Representations of the frontier orbitals. Hydrogen atoms are removed for clarity.....	65
Fig. III.13. Development of new optical bands at 565 nm and 735 nm upon addition of 10 ⁻⁴ M complex 2 to 10 equivalents of OPD in MeOH in aerobic condition. (The spectra are recorded after every 10 min). Inset: Time vs Absorbance plot at defined wavelengths	66
Fig. III.14. Rise and fall of electronic bands upon addition of 10 ⁻⁴ M complex 2 to 10 fold OPD in oxygen-saturated MeOH in aerobic condition. The spectra are recorded after every 5 min for 2.5h	67
Fig. III.15. Development of new optical bands at 565 nm and 755 nm upon addition of	

10 ⁻⁴ M complex 2 to 10 equivalents of DMOPD in MeOH in aerobic condition. (The spectra are recorded after every 10 min)	68
Fig. III.16. Rate vs conc. of OPD plot in oxygenated MeOH	69
Fig. III.17. ¹ H NMR spectrum of compound 1	70
Fig. III.18. UV-Visible spectrum of compound 1 at conc. 1×10 ⁻⁴ M	70
Fig. III.19. ESI-MS of the OPD in the presence of catalytic complex 2 in MeOH.....	71
Fig. III.20. Cyclic voltammogram of the complex 2 in methanol with 0.1 M Bu ₄ NPF ₆ at 100 mV/s scan rate	72
Fig. III.21. Cyclic voltammograms of the reaction mixture of complex 2 with 10 equivalent of OPD in MeOH under the aerobic environment with 0.1 M Bu ₄ NPF ₆ and at 100 mV/s scan-rate	73
Fig. III.22. ETS-NOCV plot of xviintermediate R1, R2 and R3. The red and blue regions of the plot denote the regions of electron depletion and accumulation, respectively	74
Fig IV.1. Schematic diagram of SARS-CoV-2	82
Fig IV.2. Representative examples of drugs comprising phenazine pharmacophore....	83
Fig. IV.3. IR spectrum of DAPH ⁺ Cl ⁻	91
Fig. IV.4. UV-Vis spectrum of DAPH ⁺ Cl ⁻	92
Fig. IV.5. ¹ H NMR spectrum of DAPH ⁺ Cl ⁻	93
Fig. IV.6. a) An ORTEP diagram of the hydrated DAPH ⁺ Cl ⁻ with 30% probability; b) Interaction map of DAPH ⁺ Cl ⁻ showing the suitability of interactions adopting the intensified red and blue regions	94
Fig. IV.7. a) Formation of a unique type of (H ₂ O) ₂ ...Cl ⁻ ...(H ₂ O) cluster through strong H...Cl, H...O and H...N interactions and its effect for the construction of supramolecular architecture in DAPH ⁺ Cl ⁻ along <i>bc</i> plane; Inset: π...π interactions of AB...AB type (inset); b) Interaction energies participating in the crystal of DAPH ⁺ Cl ⁻ to develop the supramolecular framework	97
Fig. IV.8. A view of Hirshfeld surfaces of DAPH ⁺ Cl ⁻ mapped over <i>d</i> _{norm} , shape index, curvedness and fragment patch	100
Fig. IV.9. 2D fingerprint plots of DAPH ⁺ Cl ⁻ with the contribution of interacting elements	100
Fig. IV.10. Antibacterial activity of phenazinium chloride against clinical microorganism	102
Fig. IV.11. TEM observation of the phenazinium chloride-untreated control	

<i>Streptococcus pneumonia</i> (left); TEM image of phenazinium chloride-treated <i>Streptococcus pneumonia</i>	102
Fig. IV.12. %Cell viability and viral inhibition activity of the phenazinium chloride on 1×10^4 VeroE6 cells	103
Fig. IV.13. Representative morphological changes were observed in 1×10^4 VeroE6 cells at the non-cytotoxic concentration of DAPH^+Cl^- and remdesivir using as revealed in Hoechst33342 staining (left) and nucleocapsid staining (right). [a to a1: VeroE6 cells infected virus treated with DAPH^+Cl^- ; b to b1: VeroE6 cells infected virus treated with remdesivir; c to c1: uninfected VeroE6 cells; d to d1: virus infected VeroE6 cells]	104
Fig. IV.14 (A) Binding motifs of DAPH^+Cl^- with the active sites of M^{pro} along with 2D and 3D modeled interactive plots showing various non-covalent interactions; (B) Binding motifs of DAPH^+Cl^- with the binding sites of nsp2 including 2D and 3D modeled interactive plots based on different non-covalent interactions; (C) Binding motifs of DAPH^+Cl^- with the binding sites of nsp7-nsp8 with 2D and 3D modeled interactive plots showing various non-covalent interactions	107
Fig. IV.15. MD simulation trajectory analysis from 100 ns time frame in triplicate displayed (A) R1 (replicate 1) RMSD plots of DAPH^+Cl^- bound M^{pro} (red), nsp2 (green) and nsp7-nsp8 (blue), R2 (replicate 2) RMSD plots of DAPH^+Cl^- bound M^{pro} (purple), nsp2 (orange) and nsp7-nsp8 (dark red), R3 (replicate 3) RMSD plots of DAPH^+Cl^- bound M^{pro} (black), nsp2 (yellow) and nsp7-nsp8 (parrot green); (B) [Replicate (1, 2, 3), left panel]: RMSF plots of DAPH^+Cl^- bound M^{pro} , [replicate (1, 2, 3), middle panel]: RMSF plots of DAPH^+Cl^- bound nsp2, and [replicate (1, 2, 3), right panel]: RMSF plots of DAPH^+Cl^- bound nsp7-nsp8. The RMSF plots of three replicates coded color (red, R1), (black R2) and (green R3). The Y axis scales were adjusted to display the individual replicate plots; (C) R1 (replicate 1) Radius of gyration (Rg) plots of DAPH^+Cl^- bound M^{pro} (red), nsp2 (green) and nsp7-nsp8 (blue), R2 (replicate 2) Radius of gyration (Rg) plots of DAPH^+Cl^- bound M^{pro} (purple), nsp2 (orange) and nsp7-nsp8 (dark red), R3 (replicate 3) Radius of gyration (Rg) plots of DAPH^+Cl^- bound M^{pro} (black), nsp2 (yellow) and nsp7-nsp8 (parrot green); (D) Binding SASA in the presence (black) and absence (red) of DAPH^+Cl^- with M^{pro} (left panel), nsp2 (middle panel) and nsp7-nsp8 (right panel). Lowering of SASA (black) signify the binding of ligand to the respective proteins	112
Fig. IV.16. MD simulation trajectory analysis from 100 ns time frame in triplicate	

displayed (A) Number of hydrogen bonds formed between DAPH⁺Cl⁻ and proteins during 100 ns simulation R1 (replicate 1) M^{pro} (red), nsp2 (green) and nsp7-nsp8 (blue); R2 (replicate 2) M^{pro} (purple), nsp2 (orange) and nsp7-nsp8 (dark red) and R3 (replicate 3) M^{pro} (black), nsp2 (yellow) and nsp7-nsp8 (parrot green); (B) 2D interaction plot of DAPH⁺Cl⁻ with M^{pro} (left panel), nsp2 (middle panel) and nsp7-nsp8 (right panel) during 100 ns of simulation. Dotted (purple) lines indicate H-bonds, amino acid residues inside sphere and H₂O displaying water bridges113

Fig. IV.17. 3D contour plots (in sheets) of correlation of non-bonded interactions from MM/GBSA trajectory of 100 ns (all 1000 frames). The principal interacting van der waal's, coulomb, H-bond, Lipo, salvation and covalent energies are displayed and compared with dG Bind in kcal/mol. (A) nsp2 with DAPH⁺Cl⁻ displayed high binding energy due to a good correlation (blue region) of dG vdW and dG Coulomb, (B) lessening of binding energy due to negative correlation of dG salvation and dG covalent energies, (C) important correlation between dG Lipo and dG H-bond toward augmenting binding energy of nsp2-DAPH⁺Cl⁻ complex; (D) nsp-7-nsp8 with DAPH⁺Cl⁻ displayed good binding energy due to considerable correlation (blue region) of dG vdW and dG Coulomb, (E) lessening of binding energy due to negative correlation of dG salvation and dG covalent energies, (F) important correlation between dG Lipo and dG H-bond toward augmenting binding energy of nsp7-nsp8 DAPH⁺Cl⁻ complex; (G) M^{pro} with DAPH⁺Cl⁻ displayed high binding energy due to significant correlation (blue region) of dG vdW and dG Coulomb, (H) lessening of binding energy due to negative correlation of dG salvation and dG covalent energies, (I) considerable correlation between dG Lipo and dG H-bond toward augmenting binding energy of M^{pro} - DAPH⁺Cl⁻ complex. Sheet colour blue indicates the highest correlation, green moderate and yellow least116

Fig. V.1. Representative examples of drugs having benzimidazole scaffold124

Fig. V.2. ¹H NMR spectrum of compound 3a (400 MHz, in CDCl₃)150

Fig. V.3. ¹H NMR spectrum of compound 3b (400 MHz, in CDCl₃)150

Fig. V.4. ¹H NMR spectrum of compound 3c (400 MHz, in CDCl₃)151

Fig. V.5. ¹H NMR spectrum of compound 3d (400 MHz, in DMSO-d₆)151

Fig. V.6. ¹H NMR spectrum of compound 3e (400 MHz, in CDCl₃)152

Fig. V.7. ¹H NMR spectrum of compound 4e (400 MHz, in CDCl₃)152

Fig. V.8. ¹H NMR spectrum of compound 3f (400 MHz, in CDCl₃).....153

Fig. V.9. ¹H NMR spectrum of compound 4g (400 MHz, in CDCl₃)153

Fig. V.10. ^{19}F NMR spectrum of compound 4g (376 MHz, in CDCl_3)	154
Fig. V.11. ^1H NMR spectrum of compound 4h (400 MHz, in CDCl_3)	154
Fig. V.12. ^1H NMR spectrum of compound 3i (400 MHz, in CDCl_3)	155
Fig. V.13. ^1H NMR spectrum of compound 4j (400 MHz, in CDCl_3)	155
Fig. V.14. ^1H NMR spectrum of compound 4k (400 MHz, in DMSO-d_6)	156
Fig. V.15. ^1H NMR spectrum of compound 4l (400 MHz, in DMSO-d_6)	156
Fig. V.16. ^1H NMR spectrum of compound 3m (400 MHz, in CDCl_3)	157
Fig. V.17. ^1H NMR spectrum of compound 6a (400 MHz, in CDCl_3)	157
Fig. V.18. ^1H NMR spectrum of compound 6b (400 MHz, in CDCl_3)	158
Fig. V.19. ^1H NMR spectrum of compound 6c (400 MHz, in CDCl_3)	158
Fig. V.20. ^1H NMR spectrum of compound 6e (400 MHz, in CDCl_3)	159
Fig. V.21. ^1H NMR spectrum of compound 7k (400 MHz, in DMSO-d_6)	159
Fig. V.22. ^1H NMR spectrum of compound 9a (400 MHz, in CDCl_3)	160
Fig. V.23. ^1H NMR spectrum of compound 9b (400 MHz, in CDCl_3)	160
Fig. V.24. ^1H NMR spectrum of compound 9c (400 MHz, in CDCl_3)	161
Fig. V.25. ^1H NMR spectrum of compound 9e (400 MHz, in CDCl_3)	161
Fig. V.26. ^1H NMR spectrum of compound 9k (400 MHz, in DMSO-d_6)	162
Fig. V.27. ^{13}C NMR spectrum of compound 3a (100 MHz, in CDCl_3)	163
Fig. V.28. ^{13}C NMR spectrum of compound 4j (100 MHz, in CDCl_3)	163
Fig. V.29. ^{13}C NMR spectrum of compound 4k (100 MHz, in DMSO-d_6)	164
Fig. V.30. ^{13}C NMR spectrum of compound 6a (100 MHz, in CDCl_3)	164
Fig. V.31. ^{13}C NMR spectrum of compound 9a (100 MHz, in CDCl_3)	165
Fig. V.32. ^{13}C NMR spectrum of compound 9k (100 MHz, in DMSO-d_6)	165
Fig. VI.1. IR spectra of H_2L^1 (left) and H_2L^2 (right)	176
Fig. VI.2. IR spectra of $\beta\text{-CD}$ and $\text{H}_2\text{L}^1\text{-}\beta\text{-CD}$ inclusion complex	178
Fig. VI.3. IR spectra of $\beta\text{-CD}$ and $\text{H}_2\text{L}^2\text{-}\beta\text{-CD}$ inclusion complex	178
Fig. VI.4. ^1H NMR spectrum of H_2L^1	180
Fig. VI.5. ^1H NMR spectrum of H_2L^2	180
Fig. VI.6. ^1H NMR spectra of $\beta\text{-CD}$, H_2L^1 , $\text{H}_2\text{L}^1\text{-}\beta\text{-CD}$ (Physical mixture) and $\text{H}_2\text{L}^1\text{-}\beta\text{-CD}$ (Inclusion complex) [From bottom to top]	183
Fig. VI.7. ^1H NMR spectra $\beta\text{-CD}$, H_2L^2 , $\text{H}_2\text{L}^2\text{-}\beta\text{-CD}$ (Physical mixture) and $\text{H}_2\text{L}^2\text{-}\beta\text{-CD}$ (Inclusion complex) [From bottom to up]	184
Fig. VI.8. 2D ROESY NMR of $\text{H}_2\text{L}^1\text{-}\beta\text{-CD}$ inclusion complex	185
Fig. VI.9. 2D ROESY NMR of $\text{H}_2\text{L}^2\text{-}\beta\text{-CD}$ inclusion complex	186

Fig. VI.10. UV-Vis spectra of H ₂ L ¹ and H ₂ L ² in aqueous medium at room Temperature	187
Fig. VI.11. ESI mass spectrum of H ₂ L ¹ in water	187
Fig. VI.12. ESI mass spectrum of H ₂ L ² in water	188
Fig. VI.13. UV-Vis spectrum of H ₂ L ¹ and H ₂ L ² in various solvents	189
Fig. VI.14. Time dependent UV-Vis spectrum of H ₂ L ¹ -β-CD complex in water	189
Fig. VI.15. Time dependent UV-Vis spectrum of H ₂ L ² -β-CD complex in water	190
Fig. VI.16. ESI mass spectra of H ₂ L ¹ - β-CD in water after 48h	190
Fig. VI.17. ESI mass spectra of H ₂ L ² - β-CD in water after 48h	190
Fig. VI.18. Spectrophotometric and spectrofluorimetric responses of the electronic bands for H ₂ L ¹ and H ₂ L ² upon addition of β-CD in aqueous ethanol medium; [A]: Changes of the electronic bands of H ₂ L ¹ upon successive addition of β-CD in aqueous ethanol medium; [B]: Fluorimetric response of H ₂ L ² with increasing concentration of β-CD in aqueous ethanol medium upon excitation at 265 nm; [C]: Spectrophotometric changes of the optical bands of H ₂ L ¹ with increasing concentration of β-CD in the aqueous ethanol medium; [D]: Emissive behaviour of H ₂ L ² upon successive addition of β-CD in aqueous ethanol medium upon excitation at 260 nm	193
Fig. VI.19. a) ORTEP diagram of H ₂ L ¹ ; b) Formation of the dimer between the H ₂ L ¹ units through strong H•••O interactions; c) Molecular dimensionality and interaction mapping diagram for H ₂ L ¹	194
Fig. VI.20.a) ORTEP diagram of the Schiff base, H ₂ L ² ; b) Formation of the 1D crystalline architecture of H ₂ L ² units through strong H•••O and C-H•••π interactions along the b axis; c) Molecular dimensionality and interaction mapping diagram for H ₂ L ²	195
Fig. VI.21. The asymmetric unit of H ₂ L ²	199
Fig. VI.22. Formation of 3D crystalline architecture for H ₂ L ² units through H•••O, π•••π interactions along the b axis	200
Fig. VI.23. Scanning electron microscopy images of H ₂ L ¹ at different Magnification	201
Fig. VI.24. Presentation of FESEM images of H ₂ L ² at different magnification	201
Fig. VI.25. EDX plot of H ₂ L ¹	201
Fig. VI.26. EDX plot of H ₂ L ²	202
Fig. VI.27. FESEM images of H ₂ L ¹ -β-CD inclusion complex	202
Fig. VI.28. FESEM images of H ₂ L ² -β-CD inclusion complex	203

Fig. VI.29. PXRD plot of the nano-crystalline H ₂ L ¹ and H ₂ L ²	203
Fig. VI.30. PXRD spectra of β-CD, H ₂ L ¹ , H ₂ L ¹ -β-CD Physical mixture and H ₂ L ¹ -β-CD inclusion complex (from Bottom to top)	205
Fig. VI.31. PXRD spectra of β-CD, H ₂ L ² -β-CD, H ₂ L ² -β-CD Physical mixture and H ₂ L ² -β-CD inclusion complex (from Bottom to top)	206
Fig. VI.32. Cytotoxic effect of both H ₂ L ¹ -β-CD and H ₂ L ² -β-CD on mcf7 and MDA-MB231 after 24 h of exposure. Cells were treated as described in the methods section and cell viability was determined using the MTT assay. Data are expressed as the mean + standard deviation of three experiments	207
Fig. VI.33. Concentration-dependent cytotoxic effect of H ₂ L ¹ -β-CD and H ₂ L ² -β-CD on MCF7 cells for 24h and 48h. Graph showing the cell percentage of live MCF-7 cells upon treatment with H ₂ L ¹ -β-CD and H ₂ L ² -β-CD compared to control. All data are expressed as mean SD of three independent experiments.* p < 0.05, ** p < 0.01, *** p < 0.001, **** p < 0.0001 compared to the control of each cell line	208
Fig. VI.34. Dose-dependent cytotoxicity measurement of H ₂ L ¹ -β-CD and H ₂ L ² -β-CD against MDA-MB-231 cells for 24 and 48h. Graph showing the live cell percentage of MDA-MB-231 cells treated with the drug compared to control. All data are expressed as mean SD of three independent experiments.* p < 0.05, ** p < 0.01, *** p < 0.001, **** p < 0.0001 compared to the control of each cell line	209
Fig. VI.35. Dose dependent cytotoxic effect measurement of H ₂ L ¹ -β-CD and H ₂ L ² -β-CD against normal human PBMCs for 24h. Live cell percentage was calculated using MTT assay of normal PBMCs cells. Graph showing the live cell percentage of PBMC cells treated with drug compared to control. All data are expressed as mean SD of three independent experiments.* p < 0.05, ** p < 0.01, *** p < 0.001, **** p < 0.0001 compared to the control of each cell line	210
Fig. VI.36. Haemolysis assay was performed against normal RBC cells. Negligible amount of hemolysis was found against different concentration of H ₂ L ¹ -β-CD and H ₂ L ² -β-CD upto 80μM. A little toxicity was shown at concentration of 100 μM. 5.67% haemolysis was shown for H ₂ L ¹ -β-CD and 5.85% haemolysis was shown for H ₂ L ² -β-CD All data are expressed as mean SD of three independent experiments. * p < 0.05, ** p < 0.01, *** p < 0.001, **** p < 0.0001 compared to the control of each cell line ...	211
Fig. VI.37. A. Cell cycle assay showing different phases of cells. The MCF-7 cells were treated with H ₂ L ¹ -β-CD and H ₂ L ² -β-CD at four best doses (10, 20, 40, 80 μM) for 24 h. Non-treated cells were used as control. DMSO is used as vehicle control and	

Methotrexate is used as a positive control. B. Bar graph represents the percentage of Sub-G0/G1 phase, G0/G1 phase, S phase and G2/M phase cells compared to control cells. Statistical analysis of the Sub-G0/G1, G0/G1, S, G2/M ratio of MCF-7 cells after treatment of H₂L¹-β-CD and H₂L²-β-CD. All data are expressed as mean SD of three independent experiments. * p < 0.05, ** p < 0.01, *** p < 0.001, **** p <0.0001 compared to the control of each cell line212

Fig. VI.38. The results of the Annexin V binding assay. The MCF-7 cells were treated with H₂L¹-β-CD and H₂L²-β-CD at four best doses (10, 20, 40, 80 μM) for 24 hour. Untreated cells were used as control. DMSO used as a vehicle control and Methotrexate used as a positive control. B. Bar graph represents the percentage of apoptotic positive cells compared to control cells. Statistical analysis of the apoptosis ratio of MCF-7 cells after treatment of H₂L¹-β-CD and H₂L²-β-CD. All data are expressed as mean SD of three independent experiments. *p< 0.05, ** p < 0.01, *** p < 0.001, **** p <0.0001 compared to the control of each cell line213

LIST OF APPENDIXES

Appendix	Page No.
I. List of Publications	221–222
II. Seminar & Symposium Attendent	223